Progress in Oceanography 212 (2023) 102986

Contents lists available at ScienceDirect

Progress in Oceanography

journal homepage: www.elsevier.com/locate/pocean

Burst events of near-inertial waves in the Beaufort Sea

Shuya Wang [a], Qun Li [b,*], Anzhou Cao [c,a], Xinyu Guo [a]

[a] Center for Marine Environmental Studies, Ehime University, Matsuyama, Japan
[b] MNR Key Laboratory for Polar Science, Polar Research Institute of China, Shanghai, China
[c] Ocean College, Zhejiang University, Zhoushan, China

ARTICLE INFO

Keywords:
Near-inertial wave
Arctic Ocean
Turbulent mixing

ABSTRACT

Based on moored observations from the Beaufort Gyre Exploration Project, seven burst events of near-inertial waves (NIWs) during September 2017-September 2018 are investigated in this study. These NIW events are divided into two groups. Four NIW events in group I are dominated by downgoing components associated with near-inertial currents in the magnitude of about 0.1 m/s. The plane-wave fitting results indicate that these NIWs have much smaller vertical wavelengths and energy fluxes than those in the mid-latitude oceans. By performing simulations with the slab model and analyzing sea ice conditions, we find that one NIW event is directly excited by the wind in the ice-free summer of 2018. Whereas, the other three NIW events are likely induced by the ice motion. For NIWs in group II, the downgoing and upgoing components are comparable in strength. The downgoing NIWs could be directly forced by the wind; whereas the upgoing ones may be related to the eddy events.The occurrence of the NIW events caused strong shears and hence smaller Richardson number, further resulting in the elevation of the energy dissipation rate. Results of this study can improve our understanding on the NIW dynamics and their influence on the mixing in the Arctic Ocean.

1. Introduction

Near-inertial waves (NIWs),which have frequencies close to the local inertial frequency, are ubiquitous in the ocean. In the global ocean, input of the wind into the near-inertial motions is 0.3–1.5 TW according to previous studies (Alford, 2001, 2003, 2020; Furuichi et al., 2008; Jiang et al.,2005; Simmons and Alford, 2012; Watanabe and Hibiya, 2002), which is generally comparable to the energy conversion from barotropic tides to internal tides (Simmons et al., 2004; Niwa and Hibiya, 2011). The breaking of NIWs causes intense turbulent mixing in the ocean, especially in the upper layers (Alford et al., 2016; Mackinnon et al., 2017; Whalen et al., 2020). Hence, NIWs are an important step in the ocean energy cascade and play a key role in the global ocean energy budget. As a result, understanding the generation, propagation, and dissipation of NIWs is of great importance.

Wind contributes the most to the generation of NIWs. In the low- and mid-latitude oceans, tropical cyclones and storms are capable of exciting strong NIWs because of their large wind stresses (Alford et al., 2016). The NIWs generated by tropical cyclones are associated with strong near-inertial currents in the magnitude of 0.1–1 m/s, and they could last for one to several weeks after the passage of the tropical cyclones (e.g., Sanford et al., 2011; Alford et al., 2012; Cao et al., 2018; Johnston et al., 2021; Löb et al., 2021). During the downward propagation of NIWs, they may interact with large-scale circulations or mesoscale eddies, leading to the occurrence of refraction or reflection and hence the redistribution of energy (Zhai et al., 2005; Byun et al., 2010; Kawaguchi et al., 2016; 2020; Jeon et al., 2019; Yu et al., 2022). In addition, other processes, such as the adjustment of frontal flows or eddies (Alford et al., 2013; Nagai et al., 2015) and flow-topography interaction (Nikurashin and Ferrari, 2010) can also give rise to NIWs in the ocean.

Compared with the mid-latitude oceans, the Arctic Ocean is largely covered by sea ice, causing the dampening of the input of wind energy into the ocean. However, over the past few decades, the Arctic Ocean has undergone rapid changes, with the warming of sea water and decline of sea ice (Serreze et al., 2007; Polyakov et al., 2017; Lind et al., 2018). As a result, there appears an increasing trend of near-inertial energy in the upper Arctic Ocean (Dosser and Rainville, 2016; Polyakov et al., 2020). Several studies have demonstrated the intensification of NIWs would lead to the enhancement of shear and energy dissipation, which further elevates the vertical heat flux (Polyakov et al., 2020; Dosser et al., 2021). This in turn modulates the sea ice budget in the Arctic Ocean. However, other observational results indicate that the increase of near-inertial

* Corresponding author.
E-mail address: liqun@pric.org.cn (Q. Li).

https://doi.org/10.1016/j.pocean.2023.102986
Received 19 September 2022; Received in revised form 26 December 2022; Accepted 3 February 2023
Available online 6 February 2023

energy does not definitely cause the elevation of energy dissipation, which could be due to the synchronous increase in vertical wavelength of NIWs and the suppression by strong stratification at intermediate depth (Rippeth et al., 2015; Lincoln et al., 2016; Fine and Cole, 2022). In other words, the role of NIWs in such "wind-ocean-ice" feedback cycle remains unclear and needs further clarification. Hence, NIWs in the Arctic Ocean are getting increasing attention by researchers.

Observational studies have been conducted to examine the NIWs in the Arctic Ocean. Their results indicate that the energy of NIWs in the Arctic Ocean is typically low, which is 1–2 orders of magnitude lower than that in the mid-latitude oceans (Halle and Pinkel, 2003; Merrifield and Pinkel, 1996; Pinkel, 2005). This can be largely attributed to the dampening effect of the sea ice. When the sea surface is covered by ice, the direct momentum transfer from the wind to NIWs is inhibited (Dosser et al., 2014; Dosser and Rainville, 2016; Cole et al., 2018). Even strong storms do not induce significant near-inertial responses in the ocean, resulting in low near-inertial energy and shears (Rainville and Woodgate, 2009; Martini et al., 2014). In contrast, during the ice-free stage, the input of wind energy is unaffected, thereby enhancing of NIWs in the upper ocean (Rainville and Woodgate, 2009; Lincoln et al., 2016; Kawaguchi et al., 2019). Apart from sea ice, weak Beta effect and shallow mixed layer in the Arctic Ocean also lead to the reduction of near-inertial energy in the mixed layer (Guthrie & Morison, 2021). Moreover, it should be noted that the semidiurnal tidal frequencies fall into the near-inertial band in the Arctic Ocean. Recently numerical results suggest that NIWs in this region can also be generated by diurnal tidal forcing over topographies due to the advection effect (Urbancic et al., 2022; Wang et al., 2022).

The occurrence of NIW events is associated with intensified turbulent mixing, and corresponding energy dissipation rates are usually much higher than those driven by double diffusion convection (Shibley et al., 2017; Polyakov et al., 2019). In the central Arctic Ocean, Fer (2014) observed an energy dissipation rate over 10^{-8} W/kg in the upper 100 m after a storm and suggested that the NIWs driven by storms are one possible reason. In addition, results of Kawaguchi et al. (2016) indicate that NIWs in the Chukchi Sea caused elevated energy dissipation below the thermocline as they propagated downward through an anticyclonic eddy. The NIW-induced turbulent mixing in the upper Arctic Ocean could increase the vertical heat flux (Rainville et al., 2011; Fine et al., 2021), and thereby transports more heat from the warm Atlantic Water into the surface layer (Meyer et al., 2017).On the whole, significant progress has been made by all the aforementioned studies. However,

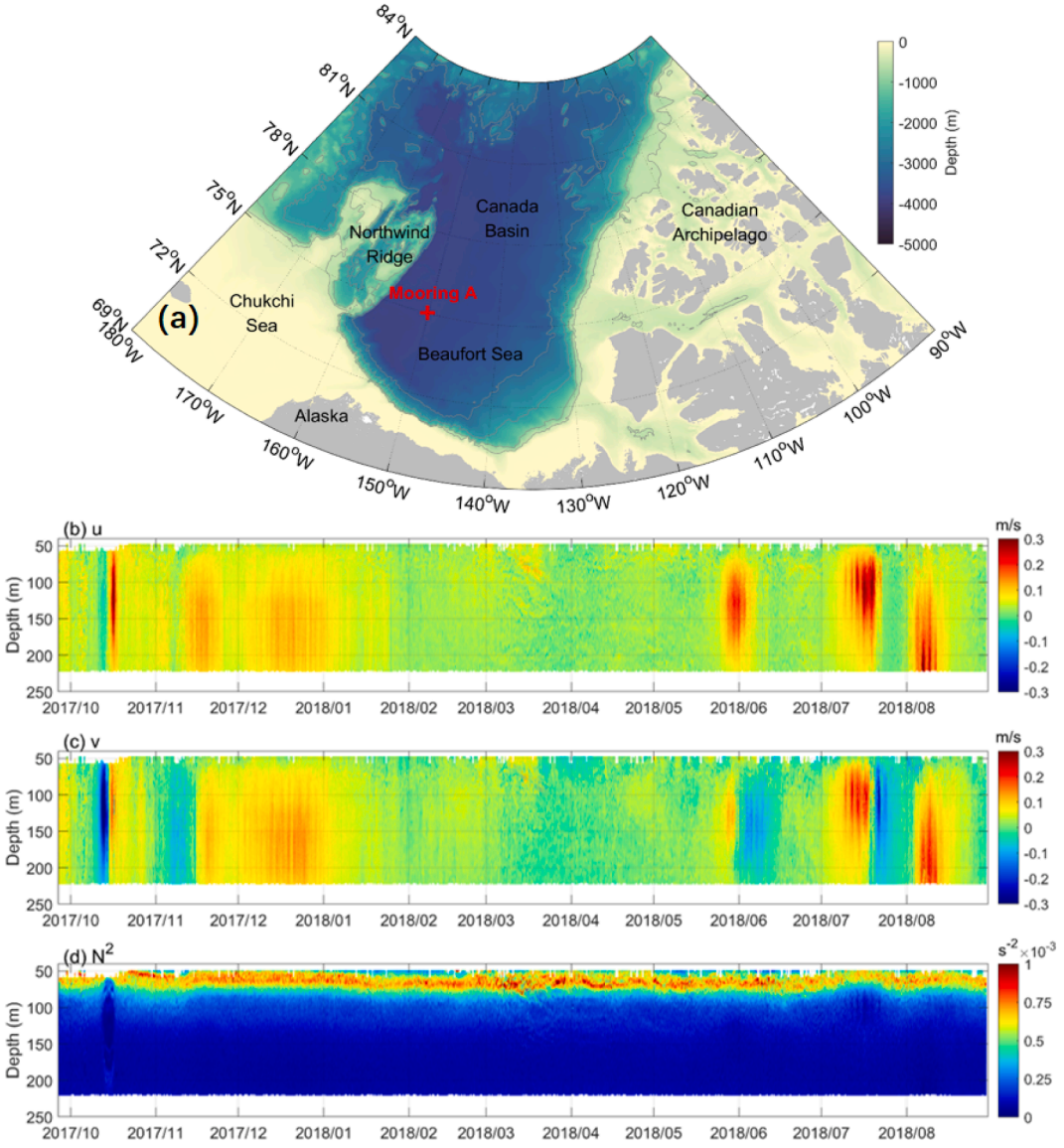

Fig. 1. (a) Bathymetry of the Beaufort Sea (shading, unit: m). Isobaths are denoted by gray contours. Location of mooring A is indicated by red plus. Raw observations of (b) zonal and (c) meridional velocities (shadings, unit: m/s) as well as (d) buoyancy frequency (shading, unit: s^{-2}).

owing to great difficulties and high costs, long-term observations with high temporal resolution are rare, making it difficult to understand the NIWs and their mechanisms lying behind in the Arctic Ocean.

The Beaufort Gyre Exploration Project (BGEP; https://www.whoi.edu/beaufortgyre; Proshutinsky et al., 2009) has deployed four moorings in the Beaufort Sea since 2003. During September 2017-September 2018, the high-frequency McLane Moored Profiler (MMP) was equipped at one mooring (Mooring A, Fig. 1a), which provides a good opportunity for us to investigate the NIWs in this region. In the study, NIW events in the Beaufort Sea observed by Mooring A are presented. Seven burst events of NIWs were recorded during the observational period. The characteristics and generation mechanisms of NIWs and their impacts on the mixing are analyzed. The remainder of this paper is organized as follows. The datasets and analyzing methods used in this study are introduced in Section 2. Observational results and corresponding interpretations are presented in Section 3. Finally, the paper is summarized in Section 4.

2. Methodology

2.1. Data

In this study, observations at the BGEP Mooring A during September 2017-September 2018 are used (https://www2.whoi.edu/site/beaufortgyre/), which was deployed at (75°1.10′N, 150°8.43′W) in the Beaufort Sea (Fig. 1a).The MMPwas equipped to measure the currents (u, v), temperature (T), and salinity (S). Profiles within 43–223 m were taken every-three hours. The vertical resolution of the data is 2 m. Fig. 1b-d show the raw observations of horizontal velocities and buoyancy frequency calculated from T and S.

An upward-looking sonar (ULS) provided the information about ice drift speed and ice draft. Here, we use the processed data provided by the BGEP (https://www2.whoi.edu/site/beaufortgyre/data/mooring-data/mooring-data-description/). The processed ice drift speed has a temporal interval of one hour, while the daily ice draft statistics are delivered in the output data from the BGEP.

In addition to the moored observations, other datasets are also used as supplementary. The 10-m wind speed is obtained from the National Centers for Environmental Prediction Climate Forecast System Version 2 (NCEP CFSv2, https://www.hycom.org/dataserver/ncep-cfsv2). The data are provided hourly on a 0.2°×0.2° grid. The sea ice concentration is obtained from the Global Ocean Sea Ice Concentration Time Series REPROCESSED (https://marine.copernicus.eu/), with a spatial (temporal) resolution of 25 km (1 day). It is computed by using passive microwave data from satellites.

2.2. Data processing

NIWs are extracted by a fourth-order Butterworth filter, with a cutoff frequency of [1.75 2.15] cpd. Semidiurnal tides are contained in this band and cannot be completely separated from the NIWs. However, previous studies have suggested weak semidiurnal tidal currents in the Beaufort Sea basin (Padman and Erofeeva, 2004; Dosser et al., 2014; Martini et al., 2014; Dosser and Rainville, 2016; Fine et al., 2021), implying they make minor contributions to the filtered velocities. Thereafter, near-inertial kinetic energy and 2-m shear squared are calculated as follows:

$$KE_f = \frac{1}{2}\left(u_f^2 + v_f^2\right) \tag{1}$$

and

$$S_f^2 = \left(\frac{\partial u_f}{\partial z}\right)^2 + \left(\frac{\partial v_f}{\partial z}\right)^2 \tag{2}$$

where u_f (v_f) is the filtered zonal (meridional) near-inertial current, and z is the depth.

NIWs are decomposed into upgoing and downgoing components. We first calculate the wavenumber-frequency spectrum using the two-dimensional Fourier transform of complex velocity ($u + iv$) or shear ($u_z + iv_z$). Then, upgoing and downgoing components of the NIWs are obtained by the inverse Fourier transform of the spectral density in the four quarters of the wavenumber-frequency spectrum. This method has been widely used in previous studies (e.g., Alford et al., 2012, 2017; Cao et al., 2019; Halle and Pinkel, 2003; Kawaguchi et al., 2019). Notably, for NIWs, the propagation directions of the phase and energy are opposite in the vertical direction. To avoid confusion, here "upgoing" and "downgoing" describe the propagation directions of the NIW energy.

To explore the NIW characteristics (e.g., frequency and wavelength), plane-wave fitting is performed (Alford and Gregg, 2001; Alford et al., 2012; Cao et al., 2018). To minimize the effects of stratification, we use Wentzel–Kramers–Brillouin (WKB) scaled variables in the WKB stretched depth coordinate (Alford et al., 2012; Sun and Pinkel, 2012). The WKB stretched depth is calculated with the time-averaged stratification during the whole observational period $\overline{N(z)}$, that is,

$$z_{WKB} = \int_{43}^{z} \overline{N(z)} \Big/ N_0 dz \tag{3}$$

where N_0 is the depth-averaged value of N(z) (Alford and Gregg, 2001; Cole et al., 2018). We begin the integration at 43 m which is the upper depth range for the MMP observation. The WKB scaled velocities are calculated by,

$$(u_{WKB}, v_{WKB}) = (u, v)\sqrt{N_0/\overline{N(z)}} \tag{4}$$

Then, we fit the WKB scaled variables with the plane-wave solution by using the least-squares method, i.e.,

$$\Psi = Re\{\ \Psi_0 \exp[\mathrm{i}(\omega \mathrm{t} - \mathrm{mz}_{\mathrm{WKB}} - \phi)\ ]\} \tag{5}$$

where Ψ_0, ω and ϕ are the amplitude, frequency, and phase of the NIW, respectively.

2.3. Slab model

The Pollard-Millard slab model (Pollard and Millard, 1970) is adopted to predict the wind-driven inertial motions in the mixed layer. The governing equation for this model is

$$\frac{dZ}{dt} + (r + if_0)Z = \frac{T}{H} \tag{6}$$

where $Z = u + iv$ is the currents in the mixed-layer, f_0 is the local Coriolis frequency, r is the damping coefficient, $T = (\tau_x + i\tau_y)/H$ is the wind stress, and H is the mixed-layer depth.

The wind stress is calculated with the wind speed from CFSv2 and a wind speed-dependent C_d as in Oey et al. (2006). We solve Equation (6) by using the spectral solution method proposed by Alford (2003). The solution contains both the Ekman component Z_E and inertial currents Z_f. The former can be calculated by $Z_E = T/(r + if_0)H$, and then Z_f is obtained by $Z_f = Z - Z_E$. The inertial energy flux into the ocean is computed as the product of the wind stress and inertial currents. Following Martini et al. (2014), the slab model is adopted for both ice-free and ice-covered conditions; however, it can only model the inertial motions in an ice-free ocean.

3. Results

3.1. Overall view of NIWs

We present an overall view of the observed NIWs in this section. First of all, the seasonal dependence of NIWs can be easily found in Fig. 2a,

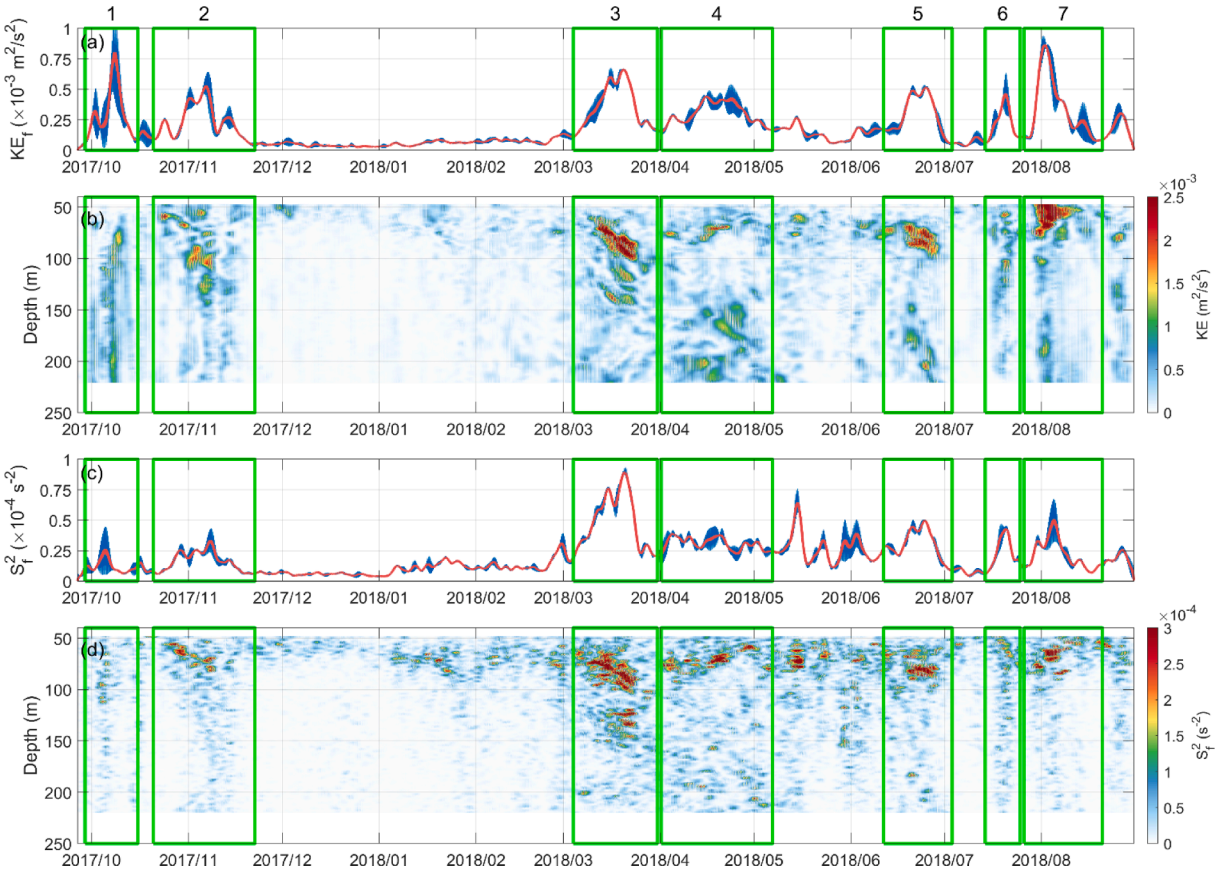

Fig. 2. (a) Depth-averaged near-inertial kinetic energy during the observational period. Blue and red lines indicate the raw and smoothed results, respectively. (b) Depth-time map of near-inertial kinetic energy (shading, unit: m^2/s^2). (c and d) Same as (a and b) but for near-inertial shear. Seven NIW events are denoted by green rectangles.

since the KE$_f$ is rather weak in the winter. Second, the KE$_f$ exhibits remarkable intermittence. Seven burst events of NIWs are identified by the pronounced peaks of KE$_f$, which occurred in spring, summer, and autumn.These observed NIWs exhibit different patterns. As shown in Fig. 2b, several NIWs are surface intensified (events 3, 5, and 7), with large KE$_f$ mainly observed in the region shallower than 100 m. But for the other events, the KE$_f$ is enhanced in the deeper region (>150 m, event 4) or basically uniform in the vertical direction (events 1, 2, and 6). In terms of the duration time, several NIW events lasted for approximately-one month (e.g., events 2, 3, 4, and 7). In contrast, the

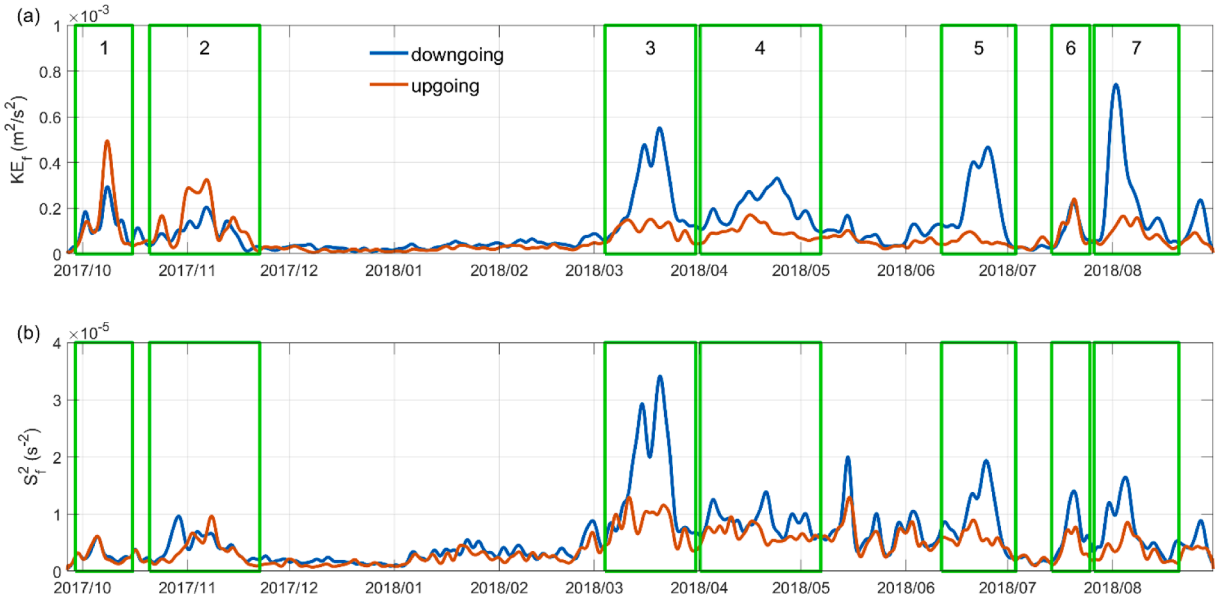

Fig. 3. (a) Depth-averaged downgoing and upgoing near-inertial kinetic energy during the observational period. (b) Same as (a) but for near-inertial shears. Seven NIW events are denoted by green rectangles. Note that "upgoing" and "downgoing" describe the propagation direction of energy.

duration time of NIW event 6 was only 11 days, which is the shortest.

As for the near-inertial shear squared, its depth-averaged result (Fig. 2c) generally shares a similar pattern to the KE_f. The strongest near-inertial shear is observed in March 2018 (event 3). However, the near-inertial shear is not highly correlated with the KE_f all the time. In other words, the NIWs with high KE_f do not cause strong shear, such as the events 1 and 2; while the peak of near-inertial shear squared also appears in May 2018 when the burst events of NIWs are absent. In addition, the near-inertial shear is basically surface intensified for almost all the events (Fig. 2d), which is different from the KE_f as analyzed above.

Then we examine the upgoing and downgoing components of the near-inertial kinetic energy and shears. As shown in Fig. 3a, the upgoing and downgoing components make different contributions to the energy for different NIW events. Based on their contributions to near-inertial energy, the seven NIW events are divided into two groups. For group I which includes events 3, 4, 5, and 7, the downgoing components are dominant, and the corresponding KE_f is at least twice as high as that of the upgoing ones (Fig. 3a). Additionally, during the four events, the downgoing components generally induce stronger shears than the upgoing ones (Fig. 3b). Nevertheless, for the other three NIW events (1, 2, and 6), the KE_f of the upgoing components is comparable to or even slightly larger than that of the downgoing ones. These NIW events are classified as group II. Similar to KE_f, near-inertial shear squared for the upgoing and downgoing components is basically at the same level (events 1 and 2), except for that in event 6 (Fig. 3b). In the following section, the two groups of NIW events are explored individually.

3.2. NIW events in group I

Group I contains four NIW events which are dominated by downgoing components. Fig. 4 displays v_f during the four events. On the whole, upward-tilting phase of velocity is clearly seen, indicating the downgoing propagation of NIW energy into the deeper ocean. For events 3 and 5, the pronounced NIW packets were radiated downward from the near-surface region (Fig. 4a and 4c). After about two weeks, the radiation penetrated to approximately 100 m, and no further downgoing radiation persisted in the deeper layers. Although the NIWs in event 7 also originated from the near-surface zone, they seem to the restricted in shallow water (<80 m). Below that, the near-inertial currents are weak (Fig. 4d). Moreover, the NIWs in event 4 show a different pattern (Fig. 4b), since the wave packet is found in the deeper layers (140–220 m). Because the temporal variation of stratification is not significant during these NIW events (Fig. 1d), such difference in the vertical structure may be due to other factors such as the non-local forcing and ice characteristics (Cao et al., 2018; Cole et al., 2018). In addition, compared with the NIWs in the mid-latitude oceans which can propagate downward deeper than 800 m (Alford et al., 2012), the downward migration of NIW packets in the Beaufort Sea only exists in the region shallower than ~ 200 m. Similar feature of NIWs was also found in the Chukchi Sea by Rainville and Woodgate (2009). With respect to the strength of NIWs, except for those in event 4, near-inertial currents during the other three events reach 0.1 m/s. The magnitude is comparable to that previously observed in the Arctic Ocean (e.g., Rainville and Woodgate, 2009; Kawaguchi et al., 2016; 2019), but lower than that observed in the mid-latitude oceans (~0.3 m/s; e.g., Alford et al., 2012; 2017; Chen et al., 2013; Cao et al., 2018).

To further examine the characteristics of these NIWs (e.g., frequency, wavenumber, and group velocity), plane-wave fitting is adopted. Here, we use the time-averaged stratification calculated from the temperature and salinity observed by the MMP (Fig. 5a). The maximal buoyancy frequency is located at $z = 65$ m. The WKB stretched depth is shown in Fig. 5b. To minimize the errors in the calculation of the downward vertical group speed and energy flux, we use the downward components rather than the total near-inertial currents in the plane-wave fitting. Also, because NIW packets appear in different depths during these events, different depth ranges are considered in our calculation (Table 1). Moreover, event 7 is not fitted because the NIWs are surface-

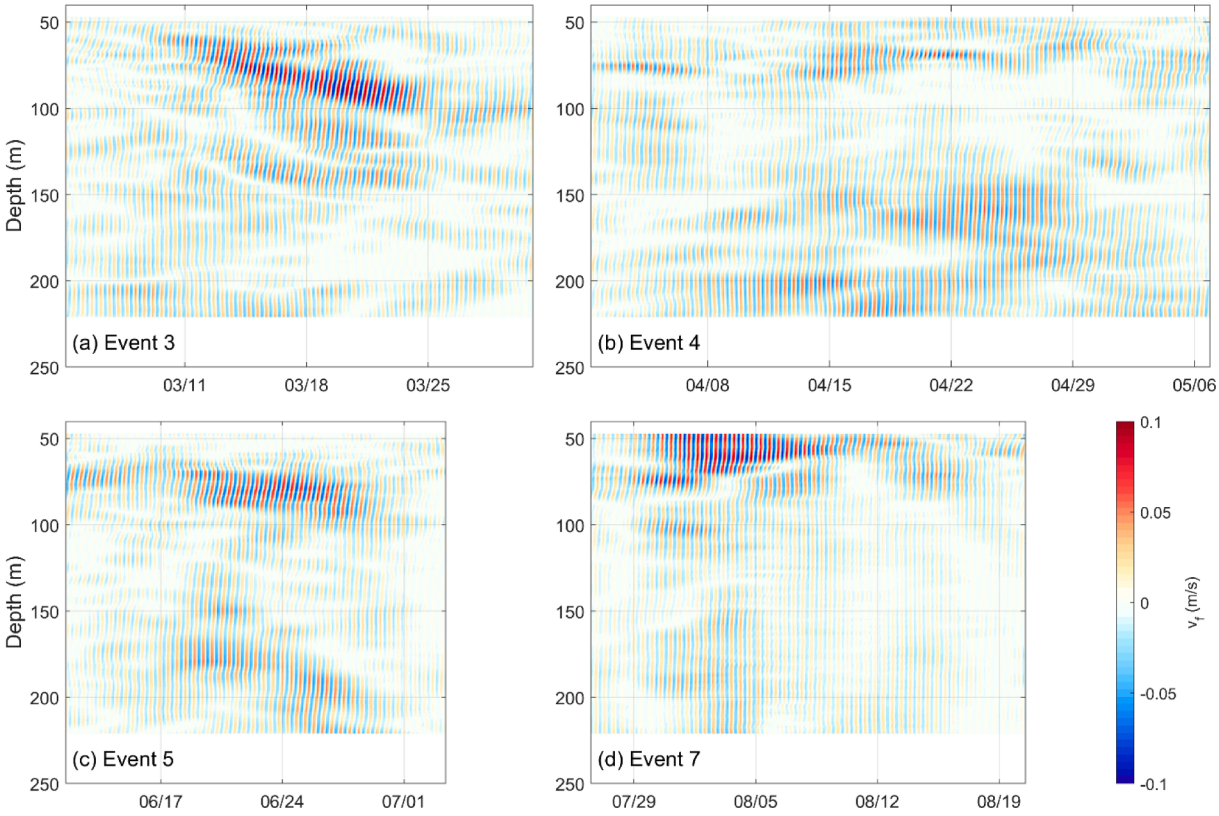

Fig. 4. Depth-time map for meridional near-inertial currents (shadings, unit: m/s) during NIW events (a) 3, (b) 4, (c) 5, and (d) 7.

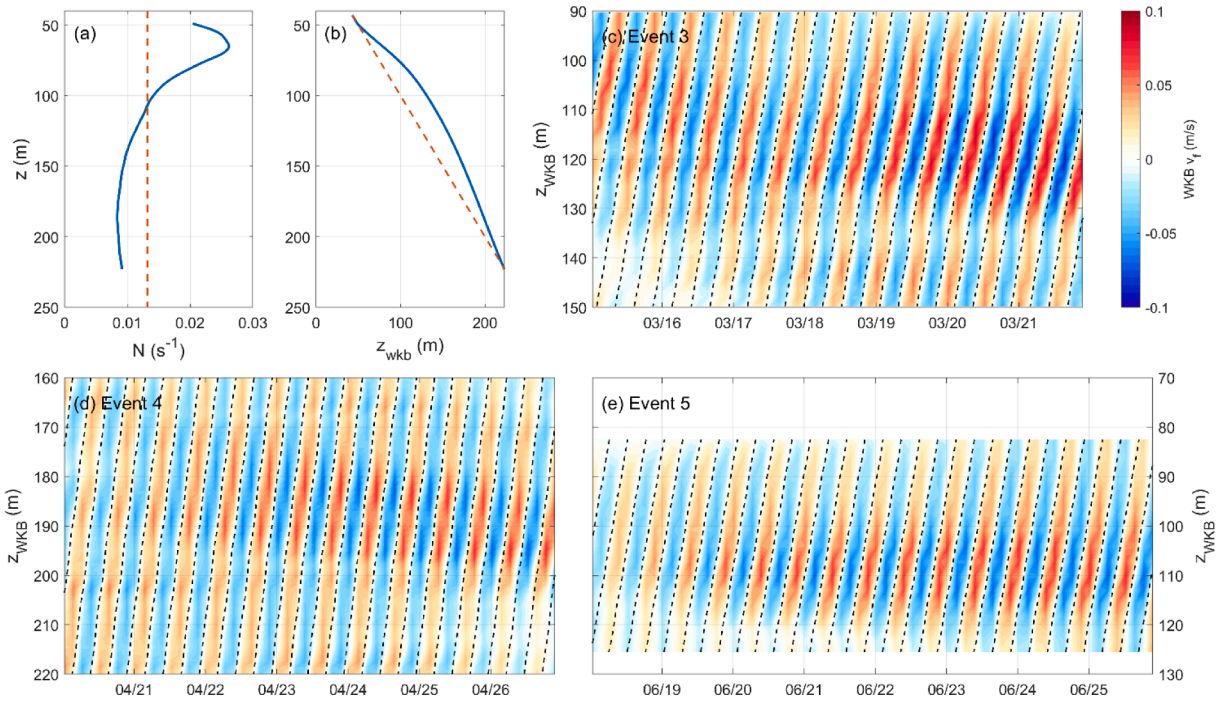

Fig. 5. (a) Time-averaged stratification during the observational period. Vertical-averaged value is indicated by vertical dashed line. (b) WKB stretched depth. The red dashed line denotes the unstretched depth for reference. (c-e) WKB scaled meridional near-inertial velocities (shadings, unit: m/s) in WKB stretched depth coordinate for NIW events 3, 4, and 5, respectively. Dashed lines in (c-e) indicate phase lines calculated by plane-wave fitting.

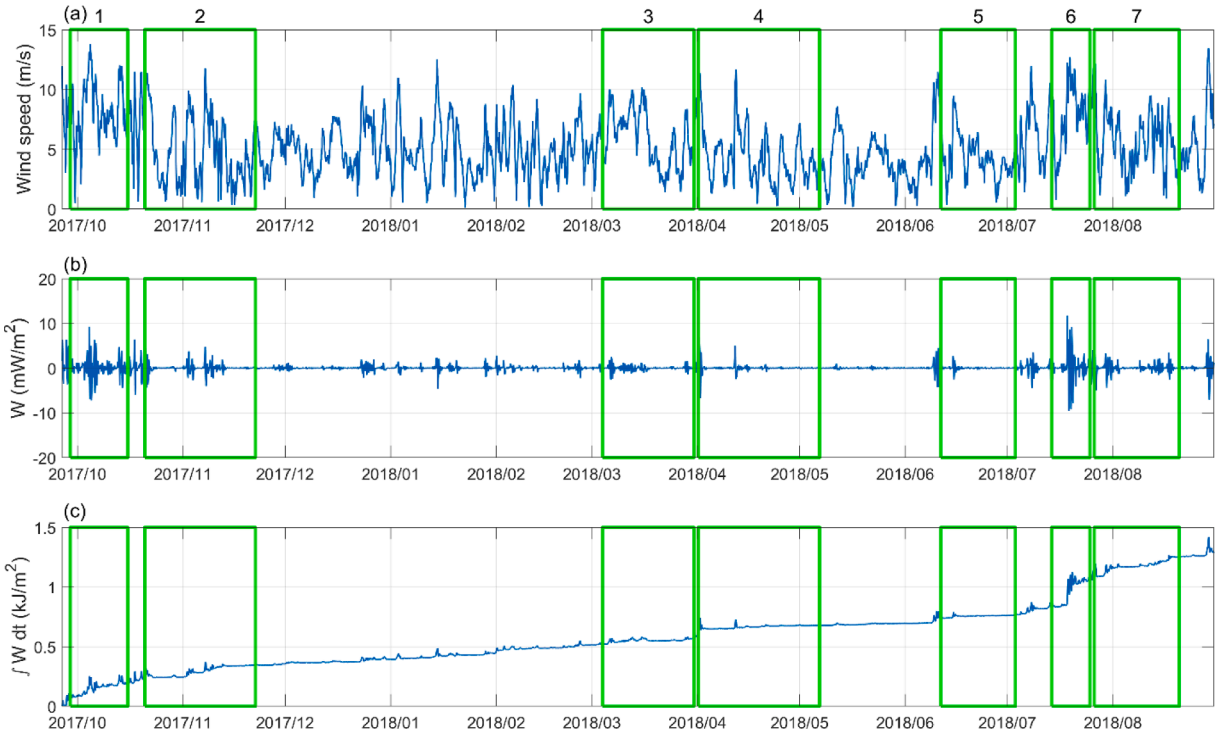

Fig. 6. (a) Time series of wind speed from NCEP CFSv2, (b) inertial energy flux and (c) cumulative energy transfer calculated by the slab model. Seven NIW events are denoted by green rectangles.

trapped. As shown in Fig. 5c-e, the near-inertial velocities are in straight phase lines after WKB stretching. The phase lines for the plane-wave fitting results show good consistency with the observations. The fitted results listed in Table 1 indicate that the frequencies of NIWs are close rather than exactly equal to the local inertial frequency. Red shift ($\omega < f_0$) occurred in event 3; while small blue shift ($\omega > f_0$) occurred in events 4 and 5. In terms of the vertical scale, the NIWs in the three events all have a wavelength smaller than 100 m, which is basically comparable to that previously observed by Ice-Tethered Profilers with Velocity (ITP-V) in the Beaufort Sea (Cole et al., 2018) as further evidenced by the wavenumber spectra of near-inertial shear (see supporting information). NIWs in event 4 have the largest wavelength among the three events,

Table 1
Plane wave fitting results for NIW events 3, 4 and 5. c_{gz}* is the group speed calculated by Equation (7), while c_{gz}^{+} is estimated from the downward migration of KE_f. Note that all the results are calculated with WKB scaled velocity and stretched depth.

Name	Time range	Depth range (m)	ω/f_0	m (rad/m)	L (m)	c_{gz}* (m/day)	c_{gz}^{+} (m/day)	F_v (W/m^2)
Event 3	20180315-20180322	90–150	0.98	0.14	44	–	4.0	5×10^{-5}
Event 4	20180420-20180427	160–222	1.02	0.11	59	4.1	2.7	5×10^{-5}
Event 5	20180618-20180626	80–126	1.01	0.15	42	1.0	1.2	1×10^{-5}

- Not calculated.

which is nearly 1.5 times than that in event 5. This could be the reason why the near-inertial shears in event 4 are weaker than those in the other two NIW events (Figs. 2 and 3). In other words, the variation of vertical scales of NIWs compensates the changing of KE_f and hence influences the near-inertial shear, which lowers the correlation between the near-inertial energy and shear (Fine and Cole, 2022). In addition, it should be noted that the vertical wavelength of the observed NIWs are much smaller than those observed in mid-latitude oceans as reported in previous studies [e.g., 130–300 m in the Northern Pacific (Alford, 2010; Alford et al., 2012); 260–370 m in the Northern South China Sea (Cao et al., 2018); 650 m in the Northern Atlantic (Yu et al., 2022)]. This implies that the NIWs in the Beaufort Sea would be more easily dissipated and hence are not radiated downward into the deep ocean.

With the obtained frequency and wavenumber of the NIWs, their vertical group speed is calculated by (Pinkel, 2005; Alford et al., 2012)

$$c_{gz} = \frac{\omega^2 - f_0^2}{m\omega} \tag{7}$$

Note that this equation cannot be applied for sub-inertial waves. Additionally, c_{gz} is also estimated by tracking the downgoing radiation of the WKB scaled near-inertial kinetic energy as a comparison (see supporting information) [Yu et al., 2022]. The vertical group speeds obtained by the above two methods are generally equal (Table 1). The downward propagation of near-inertial energy is the fastest during event 3 but the slowest during event 5. Additionally, the estimated vertical group speeds are much lower than those in the mid-latitude oceans, which exceed 10 m/day [13 m/day in the Northern Pacific (Alford et al., 2012); 60 m/day in the Northern Atlantic (Yu et al., 2022)]. This could be another reason why the observed NIWs in group I cannot propagate into the deep water. Furthermore, we estimate the vertical near-inertial energy flux by,

$$F_v = c_{gz} KE_f^{WKB} \tag{8}$$

As mentioned by Alford et al. (2012), $E_f \approx KE_f$ (E_f is the near-inertial energy) is an excellent assumption for near-inertial waves, which also works in the Arctic Ocean as evidenced by Cole et al. (2018). The estimated energy fluxes (Table 1) are basically comparable to those in Halle and Pinkel (2003) who calculated F_v in the Beaufort Sea using the spectral method. However, they are one order of magnitude lower than those observed in the central Arctic Ocean (Fer, 2014). Moreover, they are rather weak compared to those in the mid-latitude oceans ($\sim 10^{-3}$ W/m, Alford et al., 2012). This implies that the NIWs in the Beaufort Sea may not have influences on the mixing in the deep ocean below the pycnocline.

Based on the above results, the main characteristics of the NIWs in group I can be concluded. These NIWs are associated with downward energy radiation. During the four events, the NIWs lasted for approximately 2–4 weeks. By performing plane-wave fitting, we find that they have smaller vertical wavelength (<100 m) and induce weaker vertical energy fluxes ($\sim 10^{-5}$ W/m^2) compared with those in the mid-latitude oceans.

Then generation mechanism of NIWs in group I is investigated. Downgoing NIW packets are usually caused by the wind. Local variations in wind stress cause the divergence and convergence of horizontal currents. Thereafter, the currents pump the mixed layer to create NIWs downgoing into the ocean interior (D'Asaro, 1985; Martini et al., 2014; Alford et al., 2016). To explore whether the four NIW events in group I are caused by wind, simulations based on the slab model are conducted. Because of the lack of observations in the upper 40 m, we use a constant mixed layer depth $H = 20$ m following Kawaguchi et al. (2019). During the whole observational period, the wind speed is generally lower than 10 m/s (Fig. 6a). Also, no remarkable increase in wind speed is found during the four events. Except for those in event 7 (Fig. 6b), the inertial energy fluxes during events 3, 4, and 5 are nearly zero. Correspondingly, the cumulated energy transfer does not exhibit an increasing trend or a staircase (Fig. 6c). This result indicates that the observed downgoing near-inertial energy is not strongly correlated with the wind work except in the case of event 7. Thus, wind may not be responsible for the generation of NIWs in events 3, 4, and 5.

It should be noted that in the Arctic Ocean, the presence of sea ice considerably dampens the input of wind energy into the near-inertial motions in the ocean. Hence, examination on the ice condition during the observational period is necessary. At the mooring location, the sea ice concentration is nearly 100 % from late October 2017 to the end of June 2018. This further confirms that the NIWs in events 3, 4, and 5 cannot be directly driven by the wind. In contrast, an ice-free ocean appears in summer (event 7), suggesting that NIWs in event 7 are generated by the wind, combining with the aforementioned analysis. In addition to the wind, ice motion is another factor that could generate NIWs (McPhee and Kantha, 1989; Dosser and Rainville, 2016): The ice keels in the oceans play a similar role to the bottom topographies. During the sub-inertial motion of ice, horizontal gradients in its drift speed or bottom roughness induce a vertical velocity perturbation at the resonant inertial frequency beneath the ice keel, which further disturbs the bottom of the mixed layer depth so as to generate downgoing NIW packets. Here, the ice drifting speed is obtained from the ULS data, and part of the data is discarded because of large abnormal values. During events 3, 4, and 5, although the ice speed is not the fastest (Fig. 7b), the daily-averaged ice draft reaches its highest value (Fig. 7c). Additionally, the standard deviation of the ice draft is also elevated at the same time, which is possibly related to the short-time variation of the ice draft as ice keels or ridges pass by (Brenner et al., 2021). The above two conditions would be beneficial for generating downgoing NIWs. Therefore, the observed NIWs during these events are speculated to be induced by ice motion. Moreover, Dosser and Rainville (2016) also found that sub-inertial ice speed correlates with the amplitude of NIWs in the Beaufort Sea to an extent, particularly in autumn and winter. This implies that ice motion may play a considerable role in driving NIWs in ice-covered oceans. However, it should be noted that other factors such as the non-local forcing may also contribute to the downgoing near-inertial energy, but they could be difficult to identify using observations at only one fixed location.

Combining with the aforementioned analysis, we conclude that the generation of downgoing NIW packets in group I can be attributed to the wind and ice motion. The NIWs in event 7 during the summer of 2018 are directly driven by the wind. But for the other three events (3, 4, and 5) under the ice-covered condition, ice motion is considered to be the

Fig. 7. Time series of (a) ice concentration, (b) ice speed, (c) daily mean and STD of ice draft during the observation period. Wind speed is reduced to 1/50 and plotted in (b) as a comparison. Seven NIW events are denoted by green rectangles.

possible cause for the observed downgoing near-inertial energy.

3.3. NIW events in group II

Then attention is paid to the NIW events in group II. Differing from those in group I, the phase of near-inertial velocities is nearly vertical

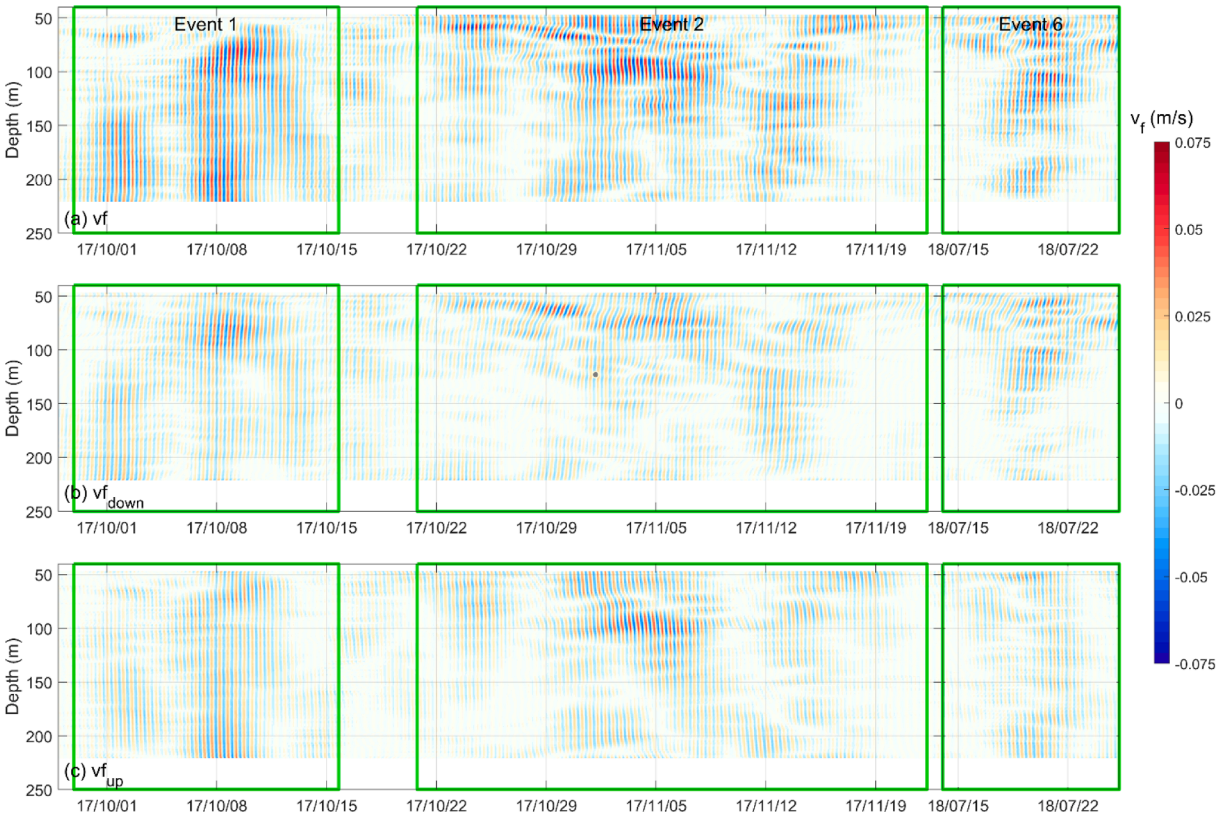

Fig. 8. (a) Meridional near-inertial currents as well as their (b) downgoing and (c) upgoing components (shadings, unit: m/s) during events 1, 2, and 6.

instead of tilting, indicating a vertical standing wave pattern (Fig. 8a). Correspondingly, the velocities for the upgoing and downgoing components are basically comparable (Fig. 8b and 8c), in accordance with the results in Section 3.1. Recalling Fig. 6, wind work is enhanced for events 1 and 6, during which the ice concentration is low. This indicates that the downgoing components of NIWs could be directly forced by the wind. Subsequently, we mainly focus on the generation mechanism of the upgoing NIWs.

The upward radiation of near-inertial energy can be attributed to several reasons. In the Arctic Ocean, numerical results indicate that upward semidiurnal (near-inertial) internal waves can be generated by diurnal tidal forcing over topographies because of the advection effect (Urbancic et al., 2022; Wang et al., 2022). However, in the central Beaufort Sea where the mooring A is located, the sea bottom is quite flat. Furthermore, tidal currents in the study region are rather week (Padman and Erofeeva, 2004). Based on the above reasons, this mechanism could not be responsible for the generation of the observed upgoing NIWs.

Previous studies have demonstrated the presence of eddies in the Beaufort Sea (Carpenter and Timmermans, 2012; Zhao and Timmermans, 2015), which may modulate the propagation of NIWs. As shown in Fig. 9a, four eddies are detected during the observational period. A strong subsurface eddy is found between events 1 and 2; while another one is observed exactly during event 6. Furthermore, by comparing the KE in the low-frequency and near-inertial bands, we find that the enhancement of upgoing KE_f is partly associated with large KE_L, indicating that their generation may be related to the eddy event (Fig. 9b). Whereas, eddy detected in June 2018 is not related to upgoing KE_f.

According to Kunze (1985), NIWs would be reflected in a positive relative vorticity field due to the increase of effective Coriolis frequency, i.e.,

$$f_{eff} = f_0 + \frac{1}{2}\zeta \tag{9}$$

where $\zeta = \frac{\partial v}{\partial x} - \frac{\partial u}{\partial y}$ is the relative vorticity. Considering that we only have data from one mooring, the poor man's vorticity (PMV) is calculated following Halle and Pinkel (2003),

$$PMV = 2\frac{\partial v_\perp}{\partial c} \tag{10}$$

in which where $v_\perp$ is the component of the low-frequency velocity perpendicular to the drift direction, and c is the along-drift coordinate. In the calculation, a frozen mesoscale field is assumed, and the data spaced in time at a fixed location are converted to space according to Zhao and Timmermans (2015). According to Fig. 9c, the strong subsurface eddy in mid-October 2017 is associated with a large Rossby number ($Ro = PMV/f_0$). However, for most of the time during NIW events 1 and 2, Ro remains at a low level. This indicates that eddy-induced relative vorticity could not be the cause of upgoing near-inertial energy during the two events. In other words, the corresponding mechanism is still unknown and needs further exploration.

In contrast, during event 6, bands for negative and positive vorticities alternate in the center of the eddy (July 2017), implying that part of the near-inertial energy would be reflected. However, it should be noted that there exist another possible mechanism resulting in the generation of upgoing NIWs. Low-frequency motions such as the eddies and fronts could give rise to NIWs whenever the geostrophic balance is not satisfied (Liang and Thurnherr, 2012; Alford et al., 2013; 2016; Nagai et al., 2015). This mechanism works if the background flows have large Rossby

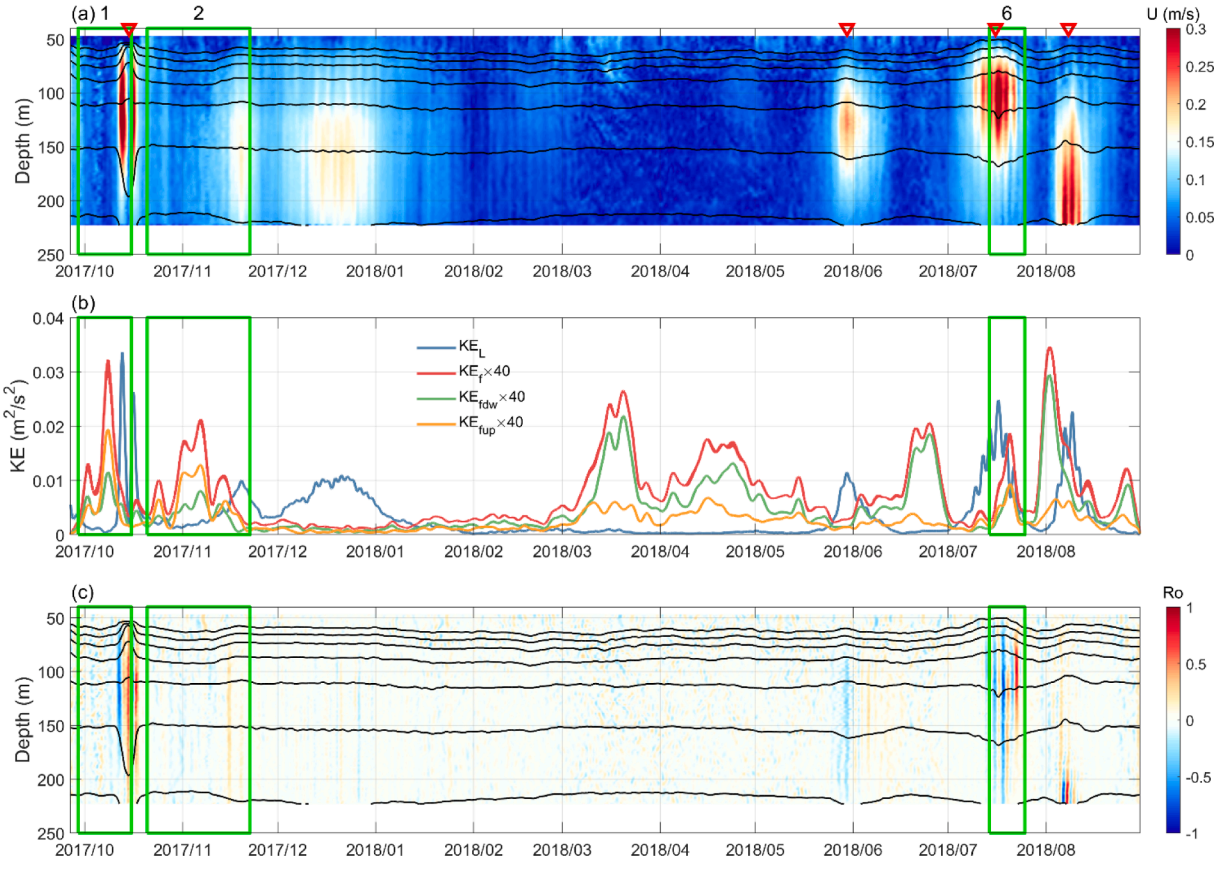

Fig. 9. (a) Depth map for low-frequency background currents (shadings, unit: m/s). Eddy events are denoted by red inverse triangles. (b) Time series of KE for low-frequency motions (blue) and NIWs (red) as well as the downgoing (green) and upgoing components (yellow). The KE of NIWs is enlarged by a factor of 40 for comparison. (c) Depth-time map for the Rossby number (PMV/f_0, shading). Black contours in (a) and (c) indicate isopycnals. NIW events 1, 2, and 6 are denoted by green rectangles.

numbers. In the Arctic Ocean, the horizontal scales of eddies are considerably smaller than those in the mid-latitude oceans (Carpenter and Timmermans, 2012; Zhao et al., 2014; Zhao and Timmermans, 2015; Wang et al., 2020). Therefore, *Ro* approaching unity is found during the eddy event in July 2018 as shown in Fig. 9c. The subsurface eddy tends to become unstable and hence excites NIWs during the adjustment process. Nevertheless, clarifying the contributions of this mechanism could be difficult with observations at only one fixed location. Future studies involving numerical simulations may be helpful in corresponding clarification.

3.4. Implications on mixing

NIWs are considered as one of the energy source of turbulent mixing in the Arctic Ocean, especially in the upper ocean (Rippeth and Fine, 2022). Considering that the observed NIWs in the Beaufort Sea have much smaller wavelengths than those in the mid-latitude oceans, they are believed to cause intense mixing. The Richardson number of the NIWs is estimated by$Ri_{NIW} = N^2/S_f^2$. During the observational period, the stratification below 50 m does not show evident seasonal variations (Fig. 1d). As a result, Ri_{NIW} is primarily determined by the near-inertial shears (Fig. 10a). Generally, the criterion for shear instability is the inverse $Ri_{\mathrm{NIW}} > 4$ (Thorpe, 2005). Here, large values of the inverse Ri_{NIW} reaching 4 are found in events 3, 4, and 5, during which the downgoing NIWs are dominant. However, for NIWs in group II, the inverse Ri_{NIW} is small, indicating a low possibility of shear instability.

Furthermore, the turbulent kinetic energy dissipation rate caused by NIWs is estimated via semi-empirical parameterization (Gregg, 1989; Kawaguchi et al., 2016). In this parameterization, the observed near-inertial shears and stratification are used, that is,

$$\varepsilon = \varepsilon_0 \left(N^2/N_0^2\right)\left(S_8^4/S_{GM}^4\right) \tag{11}$$

where the constants ε_0 and N_0 are set to 7×10^{-10} W/kg and 5.2×10^{-3}s^{-1}, respectively; S_8 is the 8-m near-inertial shears. The shear in the GM spectrum is given by

$$S_{GM}^2 = \frac{3}{2}\pi j_* E_{GM} b N_0^2 k_{crit} (N/N_0)^2 \tag{12}$$

where j_*=3 is the vertical mode number, b = 1300 m is the scale depth of thermocline, the critical wavenumber is set to $k_{\mathrm{crit}} = 0.6$ rad/s, and the non-dimensional energy level $E_{\mathrm{GM}} = 6.3 \times 10^{-5}$. Note that all the above constants are the same as those in Kawaguchi et al. (2016), who used this parameterization to estimate the NIW-induced energy dissipation in the Chukchi Sea. The result shown in Fig. 10b is generally comparable to that estimated by the fine-scale parameterization at the same location (Fine and Cole, 2022), indicating the reasonability of our calculated results. Large energy dissipation rates are observed in events 3, 4, and 5, with a magnitude over 10^{-8} W/kg. These values of ε are nearly-two orders of magnitude larger than those in the upper layers of the central Arctic Ocean (Dosser et al., 2021), suggesting that the occurrence of NIW events could drive strong mixing in the upper ocean. Additionally, some elevated dissipation rates are found beyond the periods with burst events of NIWs. This could be due to the smaller vertical scale of these weak NIWs as analyzed in Section 3.2. In contrast, ε remains at a low level during the NIW events of group II, with corresponding magnitudes lower than 10^{-10} W/kg.

Turbulent mixing drives vertical heat fluxes and thereby has the potential to modulate the sea ice budget in the Arctic Ocean (Rippeth et al., 2015; Meyer et al., 2017; Fine and Cole, 2022). Here, we calculate the vertical heat flux induced by the NIWs using the following equation,

$$Fh_{NIW} = -\rho_0 C_p K z_{NIW} \frac{\partial T}{\partial z} \tag{13}$$

where $\rho_0 = 1025$ kg/m^3 is the seawater density, $C_{\mathrm{p}} \approx 3991.9$ J/kg/K is the specific heat of sea water and $Kz_{NIW} = 0.2\varepsilon_{NIW}/N^2$ is the diapycnal

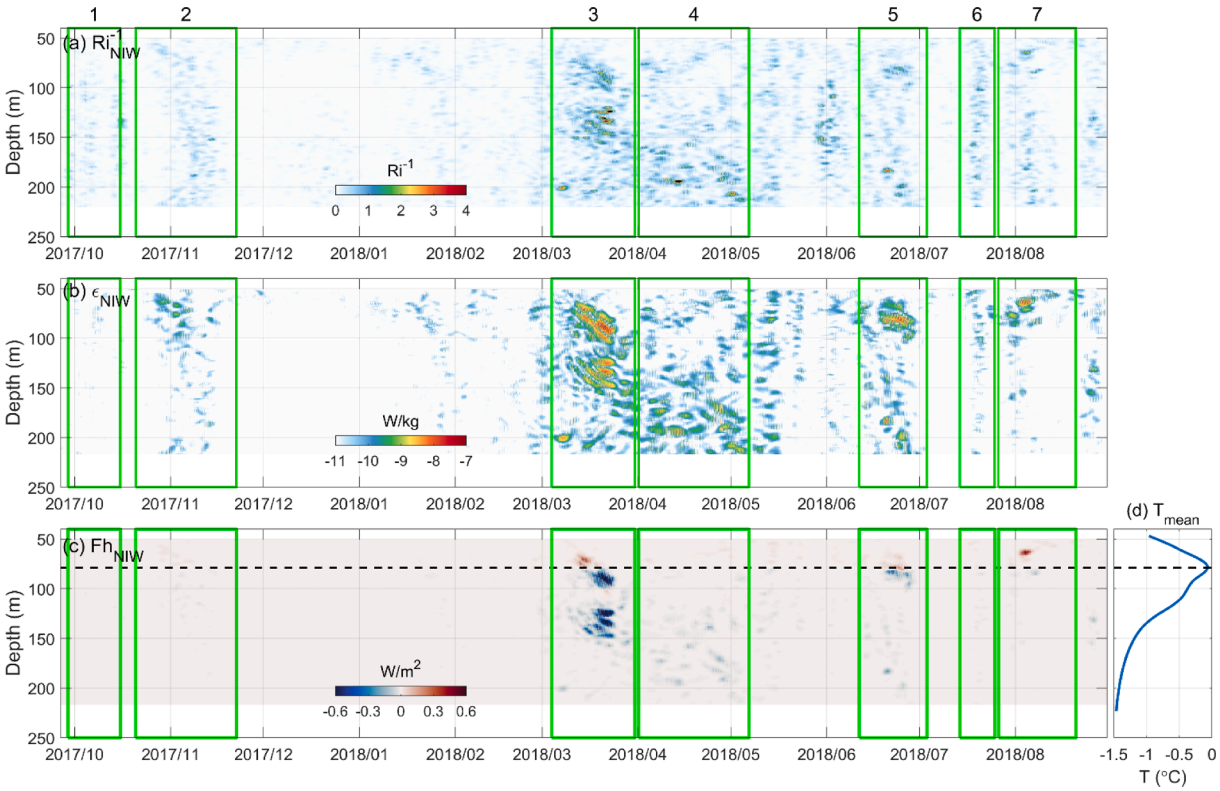

Fig. 10. Depth-time map for (a) the inverse gradient Richardson number Ri^{-1} (shading), (b) energy dissipation rate (log form, shading, unit: W/kg) and vertical heat flux (shading, unit: W/m^2) induced by NIWs. (d) Time-averaged temperature profiles. In (c) and (d), the horizontal dashed lines indicate the depth with zero vertical gradient of temperature. Seven NIW events are denoted by green rectangles in (a-c).

diffusivity caused by NIWs. Due to the limited vertical range of the high-frequency MMP observations, only the warm Pacific Water is observed, whose intrusion causes a local maximum of temperature at a depth of approximately 80 m (Fig. 10d) (Toole et al., 2010). The warm Atlantic Water cannot be found as it stays always below a depth of 200 m (Lincoln et al., 2016). Because the vertical temperature gradients above and below the warmest layer are opposite, bidirectional heat fluxes are presented in the calculated results, which are enhanced during some burst events of NIWs (Fig. 10c). In other words, NIW-induced mixing transports the heat upward and downward so as to cool the layers of warm Pacific Water, especially in event 3. In addition, the estimated Fh_{NIW} is preliminarily comparable to those in the Beaufort Sea and Canadian Basin reported by previous studies (Dosser et al., 2021; Son et al., 2022). The above result suggests an important role of NIWs in modulating the heat content in the upper Arctic Ocean.

4. Summary

NIWs are widespread in the Arctic Ocean, which have a great influence on the turbulent mixing in this region, especially in the upper layers. In this study, NIWs in the Beaufort Sea are explored by analyzing the high-frequency MMP observations from the BEGP. During the observational period (September 2017-September 2018), Seven burst events of NIWs are captured. They are divided into two groups based on their energy propagation properties.

NIWs in group I (events 3, 4, 5, and 7) are dominated by downgoing energy propagation, associated with near-inertial currents in a magnitude of 0.1 m/s. By performing plane-wave fitting, we find that the wavelengths of these NIWs are approximately 40–70 m, which are much smaller than those in the mid-latitude oceans. The downward near-inertial energy flux is in a magnitude of 10^{-5} W/m^2. This agrees with previous observations in the Beaufort Sea (Halle and Pinkel, 2003), but is at least one order of magnitude lower than those in the central Arctic Ocean (Fer, 2014) and mid-latitude oceans (Alford et al., 2013; Yu et al., 2022). The generation mechanisms for the four NIW events are different. Event 7 occurred in summer under an ice-free condition, which is excited by the wind by conducting simulation with the slab model. The other three events (3, 4, and 5) are found in the ice-covered stage. Large ice draft associated with high daily variability is observed during these events, indicating that these NIWs are likely generated due to the ice motion.

As for the NIW events (1, 2, and 6) in group II, the upgoing and downgoing components become comparable. The results of the slab model suggest that the downgoing components could be generated by the wind in an ice-free stage. However, how the upgoing ones are generated remains unclear. During events 1 and 2, the low relative vorticity is observed for most of the time, suggesting that the upgoing NIWs are unlikely to be correlated with eddies. In contrast, the presence of positive relative vorticity during event 6 implies that part of the downgoing near-inertial energy may be reflected. Moreover, given that the NIW events occurred during the passage of an eddy, they may also be generated due to the adjustment of the eddy because of their large Rossby number (~1). However, the contributions of the two mechanisms remain unknown and require further exploration in future studies.

The occurrence of NIW events has strong implications on turbulent mixing. High inverse Richardson numbers associated with the near-inertial shears are found to approach 4 during strong NIW events, implying the possibility of the occurrence of shear instability. Furthermore, the energy dissipation rate of NIWs is estimated by a semi-empirical parameterization, whose magnitude reaches as high as 10^{-8} W/kg. The enhancement of turbulent mixing by NIWs would influence the vertical heat and nutrient flux in the upper Arctic Ocean, hence further modulating the sea ice budget in this region (Dosser and Rainville, 2016; Schulz et al., 2022). We hope that the findings of this study can provide valuable insights on NIW dynamics in the Arctic Ocean.

Declaration of Competing Interest

The authors declare that they have no known competing financial interests or personal relationships that could have appeared to influence the work reported in this paper.

Data availability

Data will be made available on request.

Acknowledgements

Observational data were collected and made available by the Beaufort Gyre Exploration Program based at the Woods Hole Oceanographic Institution (https://www2.whoi.edu/site/beaufortgyre/) in collaboration with researchers from Fisheries and Oceans Canada at the Institute of Ocean Sciences. Insightful comments from the two reviewers are gratefully acknowledged.

This study was supported by the National Key Research and Development Plan of China (No.2019YFE0105700), the National Natural Science Foundation of China (No.42176244), the China Scholarship Council (No. 202006325025) and the CAS Key Deployment Project of Centre for Ocean Mega-Research of Science (No. COMS2020Q07).

Appendix A. Supplementary material

Supplementary data to this article can be found online at https://doi.org/10.1016/j.pocean.2023.102986.

References:

Alford, M.H., 2001. Internal swell generation: the spatial distribution of energy flux from the wind to mixed layer near-inertial motions. J. Phys. Oceanogr. 31, 2359–2368.
Alford, M.H., 2003. Improved global maps and 54-year history of wind-work on ocean inertial motions. Geophys. Res. Lett. 30.
Alford, M.H., 2010. Sustained, full-water-column observations of internal waves and mixing near mendocino escarpment. J. Phys. Oceanogr. 40, 2643–2660.
Alford, M.H., 2020. Global calculations of local and remote near-inertial-wave dissipation. J. Phys. Oceanogr. 50, 3157–3164.
Alford, M.H., Cronin, M.F., Klymak, J.M., 2012. Annual cycle and depth penetration of wind-generated near-inertial internal waves at ocean station papa in the northeast pacific. J. Phys. Oceanogr. 42, 889–909.
Alford, M.H., Gregg, M.C., 2001. Near-inertial mixing: modulation of shear, strain and microstructure at low latitude. J. Geophys. Res. 106, 16947–16968.
Alford, M.H., Shcherbina, A.Y., Gregg, M.C., 2013. Observations of near-inertial internal gravity waves radiating from a frontal Jet. J. Phys. Oceanogr. 43, 1225–1239.
Alford, M.H., MacKinnon, J.A., Simmons, H.L., Nash, J.D., 2016. Near-inertial internal gravity waves in the ocean. Ann. Rev. Mar. Sci. 8, 95–123.
Alford, M.H., MacKinnon, J.A., Pinkel, R., Klymak, J.M., 2017. Space-Time Scales of Shear in the North Pacific. J. Phys. Oceanogr. 47, 2455–2478.
Brenner, S., Rainville, L., Thomson, J., Cole, S., Lee, C., 2021. Comparingobservations and parameterizations of ice-ocean drag through an annual cycle across the Beaufort Sea. J. Geophys. Res. Oceans 126 e2020JC016977.
Byun, S., Park, J.J., Chang, K., Schmitt, R.W., 2010. Observation of near-inertial wave reflections within the thermostad layer of an anticyclonic mesoscale eddy. Geophys. Res. Lett. 37, L01606.
Cao, A., Guo, Z., Song, J., Lv, X., He, H., Fan, W., 2018. Near-inertial waves and their underlying mechanisms based on the south china sea internal wave experiment (2010–2011). J. Geophys. Res. Oceans 123, 5026–5040.
Cao, A., Guo, Z., Wang, S., Chen, X., Lv, X., Song, J., 2019. Upper ocean shear in the northern South China Sea. J. Oceanogr. 75, 525–539.
Carpenter, J.R., Timmermans, M.L., 2012. Deep mesoscale eddies in the Canada Basin, Arctic Ocean. Geophys. Res. Lett. 39, L20602.
Chen, G., Xue, H., Wang, D., Xie, Q., 2013. Observed near-inertial kinetic energy in the northwestern South China Sea. J. Geophys. Res. 118, 4965–4977.
Cole, S.T., Toole, J.M., Rainville, L., Lee, C.M., 2018. Internal waves in the arctic: influence of ice concentration, ice roughness, and surface layer stratification. J. Geophys. Res. Oceans 123, 5571–5586.
D'Asaro, E., 1985. The energy flux from thewind into near-inertial motions in the surface mixed layer. J. Phys. Oceanogr. 15, 1043–1049.
Dosser, H.V., Rainville, L., 2016. Dynamics of the changing near-inertial internal wave field in the arctic ocean. J. Phys. Oceanogr. 46, 395–415.
Dosser, H.V., Rainville, L., Toole, J.M., 2014. Near-inertial internal wave field in the canada basin from ice-tethered profilers. J. Phys. Oceanogr. 44, 413–426.
Dosser, H.V., Chanona, M., Waterman, S., Shibley, N.C., Timmermans, M.L., 2021. Changes in internal wave-driven mixing across the arctic ocean: finescale estimates from an 18-Year Pan-Arctic Record. Geophys. Res. Lett. 48 e2020GL091747.

Fer, I., 2014. Near-inertial mixing in the central arctic ocean. J. Phys. Oceanogr. 44, 2031–2049.
Fine, E.C., Alford, M.H., MacKinnon, J.A., Mickett, J.B., 2021. Microstructure mixing observations and finescale parameterizations in the beaufort sea. J. Phys. Oceanogr. 51, 19–35.
Fine, E.C., Cole, S.T., 2022. Decadal observations of internal wave energy, shear, and mixing in the western Arctic Ocean. J. Geophys. Res. Oceans 127 e2021JC018056.
Furuichi, N., Hibiya, T., Niwa, Y., 2008. Model-predicted distribution of wind-induced internal wave energy in the world's oceans. J. Geophys. Res. 113. C09034.
Gregg, M.C., 1989. Scaling turbulent dissipation in the thermocline. J. Geophys. Res. 94, 9686–9698.
Guthrie, J.D., Morison, J.H., 2021. Not just sea ice: other factors important to near-inertial wave generation in the arctic ocean. Geophys. Res. Lett. 48 e2020GL090508.
Halle, C., Pinkel, R., 2003. Internal wave variability in the Beaufort Sea during the winter of 1993/1994. J. Geophys. Res. 108.
Jeon, C., Park, J., Nakamura, H., Nishina, A., Zhu, X., Kim, D.G., Min, H.S., Kang, S.K., Na, H., Hirose, N., 2019. Poleward-propagating near-inertial waves enabled by the western boundary current. Sci. Rep. 9.
Jiang, J., Lu, Y., Perrie, W., 2005. Estimating the energy flux from the wind to ocean inertial motions: the sensitivity to surface wind fields. Geophys. Res. Lett. 32, L15610.
Johnston, T.M.S., Wang, S., Lee, C.Y., Moum, J.N., Rudnick, D.L., Sobel, A., 2021. Near-inertial wave propagation in the wake of super typhoon mangkhut: measurements from a profiling float array. J. Geophys. Res. Oceans 126 e2020JC016749.
Kawaguchi, Y., Nishino, S., Inoue, J., Maeno, K., Takeda, H., Oshima, K., 2016. Enhanced diapycnal mixing due to near-inertial internal waves propagating through an anticyclonic eddy in the ice-free chukchi plateau. J. Phys. Oceanogr. 46, 2457–2481.
Kawaguchi, Y., Itoh, M., Fukamachi, Y., Moriya, E., Onodera, J., Kikuchi, T., Harada, N., 2019. Year-round observations of sea-ice drift and near-inertial internal waves in the Northwind Abyssal Plain, Arctic Ocean. Polar Sci. 21, 212–223.
Kawaguchi, Y., Wagawa, T., Igeta, Y., 2020. Near-inertial internal waves and multiple-inertial oscillations trapped by negative vorticity anomaly in the central Sea of Japan. Prog. Oceanogr. 181, 102240.
Kunze, E., 1985. Near-inertial wave propagation in geostrophic shear. J. Phys. Oceanogr. 15, 544–565.
Liang, X., Thurnherr, A.M., 2012. Eddy-modulated internal waves and mixing on a midocean ridge. J. Phys. Oceanogr. 42, 1242–1248.
Lincoln, B.J., Rippeth, T.P., Lenn, Y., Timmermans, M.L., Williams, W.J., Bacon, S., 2016. Wind-driven mixing at intermediate depths in an ice-free Arctic Ocean. Geophys. Res. Lett. 43, 9749–9756.
Lind, S., Ingvaldsen, R.B., Furevik, T., 2018. Arctic warming hotspot in the northernBarents Sea linked to declining sea-ice import. Nat. Clim. Chang. 8, 634–639.
Löb, J., Köhler, J., Walter, M., Mertens, C., Rhein, M., 2021. Time series of near-inertial gravity wave energy fluxes: the effect of a strong wind event. J. Geophys. Res. Oceans 126 e2021JC017472.
Mackinnon J. A., M. H, Alford J. K, Ansong B.K, Arbic A, Barna B. P, Briegleb F. O, Bryan M. C, Buijsman E. P, Chassignet G, Danabasoglu S, Diggs P, Gent S. M, Giffies R. W, Hallberg S. R, Jayne M, Jochum J. M, Klymak E, Kunze W. G, Large S, Legg B, Mater A. V, Melet L. M, Merchant R, Musgrave J. D, Nash N.J, Norton A, Pickering R, Pinkel K, Polzin H. L, Simmons L. C, St. Laurent O. M, Sun D. S, Trossman A. F, Waterhouse C. B, Whalen Z, Zhao 2017 CLIMATE PROCESS TEAM ON INTERNAL WAVE–DRIVEN OCEAN MIXING. *Bulletin of the American Meteorological Society,* 98, 2429-2454.
Martini, K.I., Simmons, H.L., Stoudt, C.A., Hutchings, J.K., 2014. Near-Inertial Internal Waves and Sea Ice in the Beaufort Sea*. J. Phys. Oceanogr. 44, 2212–2234.
McPhee, M.G., Kantha, L.H., 1989. Generation of internalwaves by sea ice. J. Geophys. Res. 94, 3287–3302.
Merrifield, M.A., Pinkel, R., 1996. Inertial currents in the Beaufort Sea: observations of response to wind and shear. J. Geophys. Res. Oceans 101, 6577–6590.
Meyer, A., Fer, I., Sundfjord, A., Peterson, A.K., 2017. Mixing rates and vertical heat fluxes north of Svalbard from Arctic winter to spring. J. Geophys. Res. Oceans 122, 4569–4586.
Nagai, T., Tandon, A., Kunze, E., Mahadevan, A., 2015. Spontaneous generation of near-inertial waves by the kuroshio front. J. Phys. Oceanogr. 45, 2381–2406.
Nikurashin, M., Ferrari, R., 2010. Radiation and dissipation of internal waves generated by geostrophicmotions impinging on small-scale topography: theory. J. Phys. Oceanogr. 40, 1055–1074.
Niwa, Y., Hibiya, T., 2011. Estimation of baroclinic tide energy available for deep ocean mixing based on three-dimensional global numerical simulations. J. Oceanogr. 67, 493–502.
Oey, L.-Y., Ezer, T., Wang, D.-P., Fan, S.-J., Yin, X.-Q., 2006. Loop Current warming by Hurricane Wilma. Geophys. Res. Lett. 33, L08613.
Padman, L., Erofeeva, S., 2004. A barotropic inverse tidal model for the Arctic Ocean. Geophys. Res. Lett. 31, L02303.
Pinkel, R., 2005. Near-inertial wave propagation in the western arctic. J. Phys. Oceanogr. 35, 645–665.
Pollard, R.T., Millard, R.C., 1970. Comparison between observed and simulated wind-generated inertial oscillations.*Deep-Sea*. Research 17, 813–821.
Polyakov, I.V., Pnyushkov, A.V., Alkire, M.B., Ashik, I.M., Baumann, T.M., Carmack, E. C., Goszczko, I., Guthrie, J., Ivanov, V.V., Kanzow, T., Krishfield, R., Kwok, R., Sundfjord, A., Morison, J., Rember, R., Yulin, A., 2017. Greater role for Atlantic inflows onsea-ice loss in the Eurasian Basin of the Arctic Ocean. Science 356, 285–291.
Polyakov, I.V., Padman, L., Lenn, Y.D., Pnyushkov, A., Rember, R., Ivanov, V.V., 2019. Eastern arctic ocean diapycnal heat fluxes through large double-diffusive steps. J. Phys. Oceanogr. 49, 227–246.
Polyakov, I.V., Rippeth, T.P., Fer, I., Baumann, T.M., Carmack, E.C., Ivanov, V.V., Janout, M., Padman, L., Pnyushkov, A.V., Rember, R., 2020. Intensification of near-surface currents and shear in the eastern arctic ocean. Geophys. Res. Lett. 47.
Proshutinsky, A., Krishfield, R., Timmermans, M.-L., Toole, J., Carmack, E., McLaughlin, F., Williams, W.J., Zimmermann, S., Itoh, M., Shimada, K., 2009. Beaufort Gyre freshwater reservoir: State and variability from observations. J. Geophys. Res. Oceans 114, C00A10.
Rainville, L., Woodgate, R.A., 2009. Observations of internal wave generation in the seasonally ice-free Arctic. Geophys. Res. Lett. 36, L23604.
Rainville, L., Lee, C.M., Woodgate, R.A., 2011. Impact of wind-driven mixing in the Arctic Ocean. Oceanography 24, 136–145.
Rippeth, T.P., Fine, E.C., 2022. Turbulent mixing in a changing Arctic Ocean. Oceanography 35, 66–75.
Rippeth, T.P., Lincoln, B.J., Lenn, Y.D., Green, J.A., Sundfjord, A., Bacon, S., 2015. Tide-mediated warming of Arctic halocline by Atlanticheat fluxes over rough topography. Nat. Geosci. 8, 191–194.
Sanford, T.B., Price, J.F., Girton, J.B., 2011. Upper-ocean response to hurricane frances (2004) observed by profiling EM-APEX Floats*. J. Phys. Oceanogr. 41, 1041–1056.
Schulz, K., Lincoln, B., Povazhnyy, V., Rippeth, T., Lenn, Y.-D., Janout, M., et al., 2022. Increasing nutrient fluxes and mixing regime changes in the eastern Arctic Ocean. Geophys. Res. Lett. 49 e2021GL096152.
Serreze, M.C., Holland, M.M., Stroeve, J., 2007. Perspectives on the Arctic'sShrinking Sea-Ice Cover. Science 315, 1533–1536.
Shibley, N.C., Timmermans, M.L., Carpenter, J.R., Toole, J.M., 2017. Spatial variability of the Arctic Ocean's double-diffusive staircase. J. Geophys. Res. Oceans 122, 980–994.
Simmons, H.L., Alford, M.H., 2012. Simulating the long-range swell of internal wavesgenerated by ocean storms. Oceanography 25, 30–41.
Simmons, H.L., Hallberg, R.W., Arbic, B.K., 2004. Internal wave generation in a global baroclinic tide model. Deep Sea Res. Part II 51, 3043–3068.
Son, E.Y., Kawaguchi, Y., Cole, S.T., Toole, J.M., Ha, H.K., 2022. Assessment of turbulent mixing associated with eddy-wave coupling based on autonomous observations from the Arctic Canada Basin. J. Geophys. Res. Oceans 127 e2022JC018489.
Sun, O.M., Pinkel, R., 2012. Energy transfer from high-shear, low-frequency internal waves to high-frequency waves near kaena ridge. Hawaii. *J. Phys. Oceanography* 42, 1524–1547.
Thorpe, S.A., 2005. The turbulent ocean. Cambridge University Press, Cambridge, p. 485.
Toole, J.M., Timmermans, M.-L., Perovich, D.K., Krishfield, R.A., Proshutinsky, A., Richter-Menge, J.A., 2010. Influences of the ocean surface mixed layer and thermohaline stratification on Arctic Sea ice in the central Canada Basin. J. Geophys. Res. 115, C10018.
Urbancic, G.H., Lamb, K.G., Fer, I., Padman, L., 2022. The generation of linear and nonlinear internal waves forced bysubinertial tides over the yermak plateau, arctic ocean. J. Phys. Oceanogr. 52, 2183–2203.
Wang, S., Cao, A., Li, Q., Chen, X., 2022. Diurnal and semidiurnal internal waves on the southern slope of the Yermak Plateau. Sci. Rep. 12, 11682.
Wang, Q., Koldunov, N.V., Danilov, S., Sidorenko, D., Wekerle, C., Scholz, P., Bashmachnikov, I.L., Jung, T., 2020. Eddy Kinetic Energy in the Arctic Ocean From a Global Simulation With a 1-km Arctic. Geophys. Res. Lett. 47 e2020GL088550.
Watanabe, M., Hibiya, T., 2002. Global estimates of the wind-induced energy flux to inertial motions in the surface mixed layer. Geophys. Res. Lett. 29, 64-1-64-3.
Whalen, C.B., de Lavergne, C., Naveira Garabato, A.C., Klymak, J.M., MacKinnon, J.A., Sheen, K.L., 2020. Internal wave-driven mixing: governing processes and consequences for climate. Nat. rev. Earth & environ. 1, 606–621.
Yu, X., Naveira Garabato, A.C., Vic, C., Gula, J., Savage, A.C., Wang, J., Waterhouse, A. F., MacKinnon, J.A., 2022. Observed equatorward propagation and chimney effect of near-inertial waves in the midlatitude ocean. Geophys. Res. Lett. 49.
Zhai, X., Greatbatch, R.J., Zhao, J., 2005. Enhanced vertical propagation of storm-induced near-inertial energy in an eddying ocean channel model. Geophys. Res. Lett. 32.
Zhao, M., Timmermans, M., Cole, S., Krishfield, R., Proshutinsky, A., Toole, J., 2014. Characterizing the eddy field in the Arctic Ocean halocline. J. Geophys. Res. Oceans 119, 8800–8817.
Zhao, M., Timmermans, M.-L., 2015. Vertical scales and dynamics of eddies in theArctic Ocean's Canada Basin. J. Geophys. Res. Oceans 120, 8195–8209.